Aerodynamic Installation Effects of Over-the-wing Mounted Ultra-high-bypass Engines

Vinícius Tavares Silva
vincius@chalmers.se
Chalmers University of Technology
Department of Mechanics and Maritime Sciences
Gothenburg
Sweden

Anders Lundbladh
GKN Aerospace Sweden
Engine Systems
Trollhättan
Sweden

Carlos Xisto
Chalmers University of Technology
Department of Mechanics and Maritime Sciences
Gothenburg
Sweden

ABSTRACT

In order to increase propulsive efficiency and decrease specific thrust, future aeroengines for commercial airliners will have to operate with higher bypass ratios and lower fan pressure ratios. This results in a substantial increase of the fan diameter. One major issue with the conventional under-wing installation of ultrahigh-bypass engines is the limited space underneath the wings. Integrating larger engines under-the-wings could require prohibitive increase in landing gear height and weight to attain an adequate ground clearance. One potential solution is to mount the engines over-the-wings, which would eliminate the ground clearance problem and, in addition, reduce ground noise. Over-wing nacelle installation acquired a bad reputation in the past since the benefits of such configuration would be often outweighed by poor aerodynamic performance. Nonetheless, some recent studies indicate that over-wing mounted nacelles could be a feasible integration option. This paper provides an aerodynamic evaluation of an over-the-wing mounted nacelle configuration compared with an under-the-wing configuration for a mid-cruise condition. The nacelles and pylons are designed by using an in-house tool for engine aircraft aerodynamic integration. The flow field is computed by means of Reynolds-averaged Navier-Stokes equations. The effects of wing/nacelle/pylon interference are investigated, and the aerodynamic performance of each configuration is evaluated by means of thrust and drag bookkeeping. Results show that the over-the-wing nacelle installation has increased the overall drag by 19.7 drag counts, when compared to a conventional under-wing mount, which was caused mainly due to a higher wing wave drag and pylon/nacelle interference drag.

Keywords: Over-the-wing nacelle installation, propulsion integration, ultra-high bypass ratio, computational fluid dynamics, nacelle, aerodynamics

NOMENCLATURE

AoA	Angle of attack
BC	Boundary condition
BPR	Bypass-ratio
CFD	Computational fluid dynamics
CRM	Common research model
CST	Class shape transformation
MAC	Mean Aerodynamic chord
OWN	Over-the-wing nacelle
RANS	Reynolds Averaged Navier Stokes
SST	Shear stress transport
UHBPR	Ultrahigh-bypass-ratio
UWN	Under-the-wing nacelle
WB	Wing-body
WBPN	Wing-body-pylon-nacelle

Symbols

A_{ref}	Reference area
C_d	Drag coefficient
C_l	Lift coefficient
C_p	Pressure Coefficient
D_{fan}	Fan diameter
D_{nac}	Nacelle drag
D^*_{nac}	Modified nacelle drag
F_G	Gauge stream force
F_{net}	Net propulsive force
L_I	Inlet length
T^*_{net}	Modified standard net thrust
$\dot{m}$	Mass flow
$\boldsymbol{e_d}$	Unity vector in the drag direction
ϕ_{post}	Post-exit force
ϕ_{pre}	Pre-entry force
c	Chord
p	Pressure
MFR	Mass flow ratio
$\boldsymbol{V}$	Velocity vector
$\boldsymbol{n}$	Unit normal Vector
η	Spanwise wing position
θ	Circumferential position at the nacelle
ϕ	Force acting on a surface or on a streamtube boundary
$\boldsymbol{\tau}$	Shear stress tensor

1.0 INTRODUCTION

In the latest generation of new and derivative commercial airliner engines, the fan diameter and bypass-ratio (BPR) have increased to improve propulsive efficiency and reduce specific thrust, also resulting in less power needed. The power-reduction for take-off and climb leads to better matching of take-off and cruise performance, allowing further fuel consumption savings. Although the geared turbofan technology allows the BPR and fan diameter to be further increased, the conventional under-the-wing nacelle (UWN) mounting poses integration challenges such as attaining an adequate ground clearance, likely requiring a substantially longer and heavier landing gear. Another drawback of an under-wing mount is that the engines are completely exposed with respect to ground noise, which can also be amplified by airframe reflections. An over-the-wing nacelle (OWN) integration would eliminate the ground clearance problem for the next generation of ultrahigh-bypass-ratio (UHBPR) engines, as well as reduce the

likelihood of foreign object damage. Moreover, wing shielding can potentially reduce ground noise.

Overall, it is accepted that engines installed over-the-wings will be outperformed by an under-wing mount, in terms of lift and drag, assuming that the engines are optimally integrated in both configurations. This is likely caused by high pressure disturbances at the wing upper surface of the OWN configuration, leading to increased interference drag and lift penalties [1]. Despite that, a few OWN configurations had been developed, such as the Fokker 614 and the HondaJet.

Some results in the literature indicate that OWN configurations can be an aerodynamically efficient installation option, and that past evaluations might have failed to properly consider interactions between the nacelle shape and position, as well as the pylon and wing shapes. Fujino and Kawamura [2] have shown that by placing an over-wing mounted nacelle at an optimum position relative to the wing, the wave drag can be reduced and the drag divergence Mach number increased, for an OWN business jet configuration. Kimiey et al. [1] studied UWN and OWN configurations, concluding that, although the OWN provides higher interference effects, the overall drag was reduced for freestream Mach numbers above 0.78. Hill and Kandil [3] also compared OWN and UWN configurations and observed that whereas the OWN installation results in higher overall drag at cruise, its drag rise characteristics are significantly better than those of the UWN configuration. Berguin and Mavris [4] underlined the importance of considering the interaction effects between the nacelle position, nacelle shape and wing shape on the optimization of an OWN configuration, achieving a 70% drag reduction with respect to an optimization process that solely varied the nacelle position. Hooker et al. [5]. showed that the most favorable OWN position is near the wing's trailing edge, with a potential for increasing the aerodynamic efficiency up to 5%, compared to a conventional UWN configuration. On the aeroacoustics side, Lorteau et al. [6] have recently shown that an UWN configuration can be up to 12 dB noisier than an OWN configuration, at a position in front of the airplane. Furthermore, Lockheed is developing an innovative airlifter configuration, the Hybrid Wing Body, that comprises over-wing installed engines, and aims at a fuel saving of 70% compared to the C-17 airlifter [7].

Despite of the recently regained attention of OWN mounting, the installation effects of UHBPR engines over-the-wings have not yet been explored in detail, thus leading to doubts regarding the feasibility of such configurations. Modern computational fluid dynamics (CFD) techniques, combined with integrated shape and position optimization procedures, such as the studies presented in Refs. [8, 9] for UWN configurations, might be necessary to thoroughly evaluate the aerodynamics of over-wing integration. The present study aims at providing a preliminary aerodynamic evaluation of an OWN configuration comprising an advanced UHBPR engine and an ultrashort nacelle. The aerodynamic performance of a conventional UWN configuration is compared to an advanced OWN mount. The flow physics, computed by means of CFD, are studied in detail for both cases, the installation and interference effects are explored, and the feasibility of OWN configurations is discussed.

2.0 METHODOLOGY

The methods described next are integrated in a framework for aerodynamic evaluation of engine-aircraft installation. The framework is comprised of thermodynamic cycle calculation, nacelle and pylon geometry generation, integration with the wing-body (WB) aircraft geometry, automatic meshing, flow field solution via Reynolds averaged Navier stokes (RANS) equations and performance analysis by bookkeeping of thrust and drag.

2.1 Nacelle and pylon geometry generation

The nacelle shape used in the current work was generated by means of the Class Shape Transformation (CST) method [10, 11] which consists of a versatile and robust approach for parametric geometry representation. It has proven to be able to create smooth aerodynamic shapes with a small number of design variables. A CST curve is

created by means of a product between a class function and a shape function. The class function defines the basic profile, which is transformed by the shape function, normally represented by a Bernstein polynomial [10, 11].

A full 2D nacelle geometry is defined by joining six distinct CST curves, representing the fan-cowl, inlet, bypass nozzle, core nozzle, core-cowl, and plug. Figure 1a depicts the major parameters for the nacelle geometric representation. For a 3D nacelle design, two dimensional shapes are created at the positions $\psi = 0^o$, $\psi = 90^o$ and $\psi = 180^o$, respectively referred to as crown, maximum half-breadth (MHB) and keel, where, for a cylindrical coordinate system, ψ is the azimuth angle. The 3D shape is generated by performing sinusoidal interpolations in r (radial coordinate) and x (axial coordinate) between the crown, MHB, and keel. The left nacelle half ($180^o \leq \psi \leq 360^o$) is a mirror image of the right one. The core part of the nacelle and nozzles is axisymmetric. Figure 1b shows a 3D nacelle geometry representation. Turbofan nacelles can be drooped to better align the inlet with the incoming flow and reduce the drag at cruise. An example of an asymmetric nacelle with a positively drooped inlet is depicted in Figure 1c.

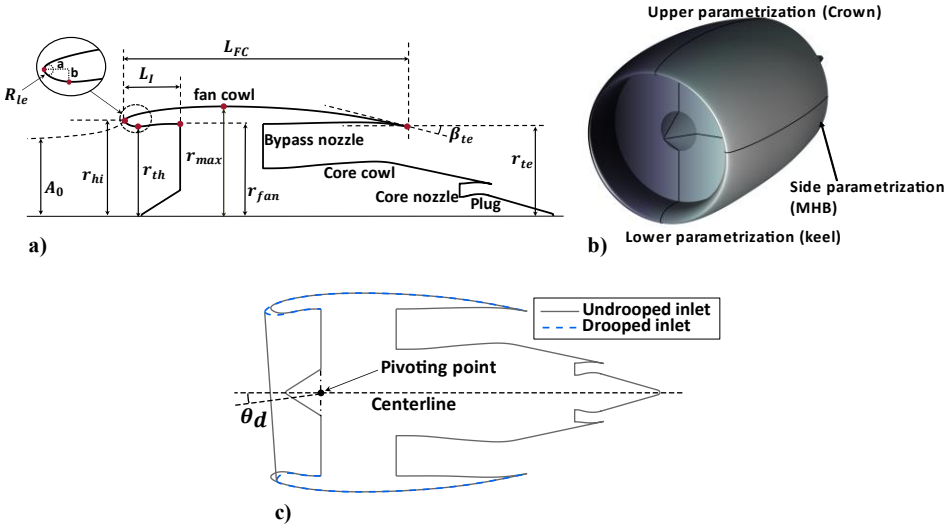

Figure 1 Nacelle geometry representation for: a) 2D nacelle profile, b) 3D asymmetric geometry and c) drooped inlet

The nacelle used in this paper features an ultra-short inlet, with inlet length to fan diameter (L_I/D_{fan}) equal to 0.3. It was designed by employing a multipoint design strategy, that considers the most critical operating conditions for the engine's performance and nacelle's design, such as cruise high angle-of-attack (AoA) and crosswind. The design strategy and some of the obtained shapes are described in Ref. [12]. For the cases presented later in this paper, an axisymmetric nacelle geometry was chosen.

The pylon geometries for both the OWN and UWN configurations are generated by vertical stacking of NACA 4-digit symmetric airfoils and are automatically adapted to nacelle position changes. The internal bifurcations were not modelled in the current study.

2.2 Aircraft geometry

The nacelle and pylons were integrated with the NASA wing-body Common Research Model (CRM) aircraft geometry, which is comprised of a modern supercritical wing and a fuselage, representative of a wide-body commercial transport aircraft [13]. The OWN mount might require a T-tail configuration, and therefore, the conventional tail of the CRM was not included. The nacelle used in this work was designed for an UHBPR engine with approximately the thrust level to power a narrow-body aircraft and thus the CRM original geometry was scaled down to the size of an A320, with respect to the mean aerodynamic chord (MAC).

The UWN configuration had its engine installed at the same axial, vertical and spanwise positions as the original CRM's nacelle, with respect to the inlet's highlight, with pitch and toe angles equal to zero. For the OWN case, the chosen engine position was based on one of the optimum cases presented in Ref. [5], where the engine is installed near the wing's trailing edge. For both the OWN and UWN configurations the nacelle was placed at 33% of the wing half-span.

2.3 Numerical approach

The commercial software POINTWISE was chosen to generate the hybrid meshes used in this work. For the surface meshes, quads and triangles were generated by means of the quad dominant algorithm. The boundary layer was meshed with a combination of anisotropic tetrahedra, pyramids, prisms, and hexahedra elements, whilst the rest of the domain was populated by using the voxel algorithm (hexahedra layers with pyramids and tetrahedra transitions). The computational domain is defined between the aircraft and a spherical far-field with radius equal to 100 times the MAC. Only half of the aircraft geometry was meshed, assuming flow field symmetry. In order to resolve the viscous sub-layer, the first cell height was set so that $y^+ < 1$. Grids with 43.76 and 44.48 million elements were produced for the OWN and UWN configurations, respectively. Figure 2 shows the OWN mesh used in this study.

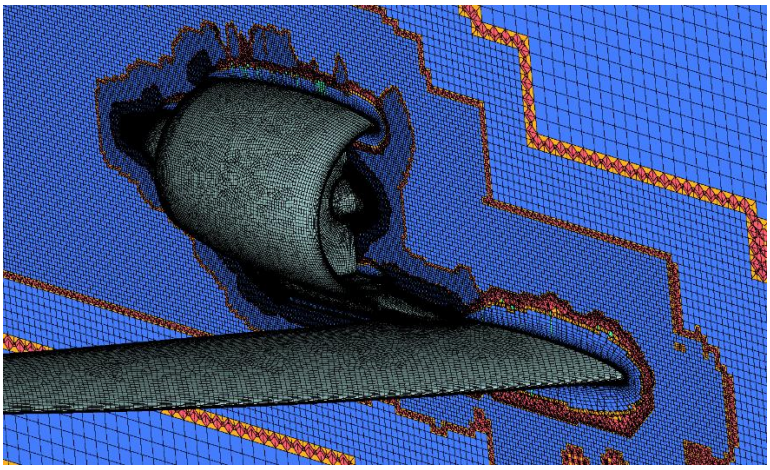

Figure 2 Hybrid mesh about the nacelle and wing for the OWN configuration. Tetrahedra, pyramids, prims and hexahedra, are shown in red, yellow, green and blue, respectively.

The utilized CFD solver was the commercial software ANSYS FLUENT. The pressure-based solver and the pressure-velocity coupled algorithm were selected to resolve the Reynolds-Averaged Navier-Stokes equations. Menter's $k-\omega$ shear stress transport (SST) model was used for turbulence closure. The flow field gradients were calculated by means of the least-squares cell-based method and a second order upwind scheme was used for spatial discretization of the momentum and energy equations.

2.3.1 Boundary conditions

The schematic representation of the computational domain and boundary conditions (BC) for the CFD simulations is shown in Figure 3. At the fan face, a pressure outlet BC is set, where constant static pressure is specified, and the mass flow is targeted. At the inlet of the bypass and core nozzles, a mass flow inlet BC was chosen, where mass flow and total temperature are set. The external domain is defined as a pressure far-field BC, where the static temperature, static pressure, Mach number and flow direction are specified. All the nacelle and aircraft surfaces were defined as no-slip adiabatic walls. The spinner was modeled as a rotating wall. The engine boundary conditions were initially calculated by carrying out a thermodynamic cycle analysis using the commercial software GASTURB, for a cycle representative of an UHBPR turbofan engine. The freestream boundary conditions were selected for a typical narrow-body aircraft operating at cruise: a flight Mach number equal to 0.8 and an altitude of 35000 ft.

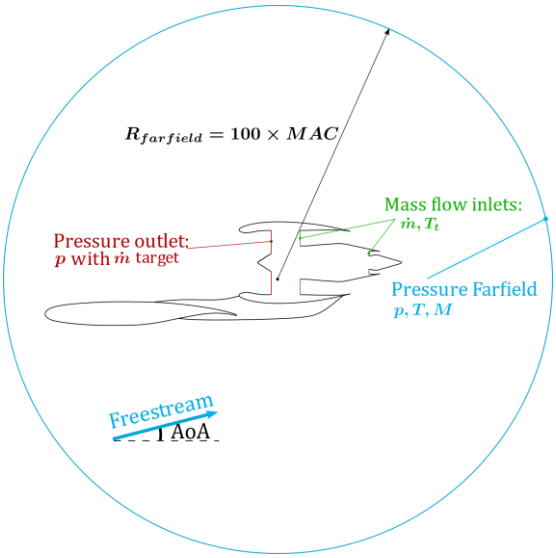

Figure 3 Boundary conditions and computational domain used in the current study

2.4 Thrust and drag bookkeeping

A modified near-field bookkeeping method, which involves integration both over the nacelle surfaces and along the captured streamtube, was employed in this work, based on the formulation presented in Ref. [14]. A schematic representation of the forces acting on a two-stream turbofan is depicted in Figure 4. The flow is not always aligned with the domains' axis, therefore, an aerodynamic reference frame must be defined. In Figure 4, *x* and *y* represent the aircraft reference frame, whereas *l* and *d* refer to the direction in which lift and drag are computed, respectively.

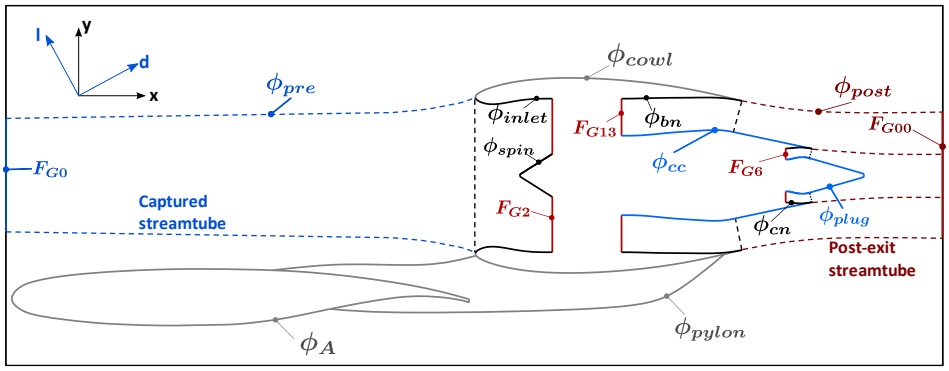

Figure 4 Forces acting on a two-stream turbofan, used for the thrust and drag bookkeeping definition

The forces acting on the nacelle, pylon and aircraft wall surfaces, as well as in the captured and post-exit streamtubes boundaries, here denoted ϕ, can be expressed as follows:

$$\phi = \iint_S [(p - p_\infty)\boldsymbol{n} + \boldsymbol{\tau} \cdot \boldsymbol{n}]\, dS \cdot \boldsymbol{e_d} \qquad (1)$$

where $\boldsymbol{e_d}$ is the unit vector in the flow direction. The stream gauge forces, denoted by F_G, can be defined as:

$$F_G = \iint_S [\rho \boldsymbol{V}(\boldsymbol{V} \cdot \boldsymbol{n}) + (p - p_\infty)\boldsymbol{n}]\, dS \cdot \boldsymbol{e_d} \qquad (2)$$

The nacelle drag D_{nac} is typically defined as the summation of the pressure and viscous forces acting on the fan cowling ϕ_{cowl} and the forces acting on the captured and post exit stream tubes ϕ_{pre} and ϕ_{post}, respectively, as follows [14]:

$$D_{nac} = \phi_{pre} + \phi_{cowl} + \phi_{post} \quad (3)$$

The major difficulty in computing drag in CFD applications comes from the accurate extraction of ϕ_{post}. Since the downstream force F_{G00} is not known, ϕ_{post} should be computed by direct integration on the post-exit streamtube boundaries. However, due to installation effects, the post-exit stream tube will be far from axisymmetric, presenting complex flow patterns, and thus posing a challenge to the direct integration method, that requires the exact geometry of the post-exit streamtube. Moreover, in order to accurately compute ϕ_{post} the mesh downstream of the nacelle must be significantly refined, increasing substantially the computational cost of the simulation. A common practice is to define a modified nacelle drag D^*_{nac} that excludes ϕ_{post}:

$$D^*_{nac} = \phi_{pre} + \phi_{cowl} \quad (4)$$

Although the definition presented in equation 4 has been used multiple times in the literature [9, 15, 16] it should be advertised that ϕ_{post} is normally a force pointing forward (thrust direction) that can have significant magnitude, as shown in Ref. [8], and therefore, neglecting such term might result in substantially overpredicting the nacelle drag.

The nacelle net propulsive force F^{NAC}_{net} can be calculated from application of the momentum conservation equation to a closed control surface surrounding the nacelle, leading to the definition presented in Eq. (5)

$$F^{NAC}_{net} = F_{G13} + F_{G6} - F_{G2} - (\phi_{bn} + \phi_{cc} + \phi_{cn} + \phi_{plug} + \phi_{cowl} + \phi_{spin} + \phi_{inlet}) \quad (5)$$

Several definitions of thrust can be found in the literature [15, 16, 14]. The definition employed here is referred to as modified standard net thrust T^*_{net}:

$$T^*_{net} = F_{G13} + F_{G6} - F_{G0} - (\phi_{bn} + \phi_{cc} + \phi_{cn} + \phi_{plug}) \quad (6)$$

where the term “modified” refers to the addition of the core cowl and plug external forces to the standard net thrust definition. The pre-entry drag is defined by applying the momentum conservation to the captured streamtube:

$$\phi_{pre} = F_{G2} - F_{G0} + \phi_{spin} + \phi_{inlet} \quad (7)$$

By substituting Eq. (6) and Eq. (7) into Eq. (5), the nacelle net propulsive force becomes:

$$F^{NAC}_{net} = T^*_{net} - \phi_{pre} - \phi_{cowl} = T^*_N - D^*_{nac} \quad (8)$$

The aircraft net force F_{net} and overall drag D_{WBPN} can be defined with the inclusion of the pressure and skin friction forces acting on the airframe and pylon:

$$F_{net} = T^*_{net} - \phi_{pre} - \phi_{cowl} - \phi_{pylon} - \phi_A = T^*_{net} - D^*_{nac} - \phi_{pylon} - \phi_A \quad (9)$$

$$D_{WBPN} = D^*_{nac} + \phi_{pylon} + \phi_A \quad (10)$$

The installation drag D_{inst} is defined by subtracting the wing-body drag D_{WB} from the wing-body-pylon-nacelle configuration drag D_{WBPN}, for a fixed lift coefficient C_l. D_{WB} can be calculated by simply integrating the pressure and shear forces at the isolated wing-body configuration surfaces (Eq. (1)), whereas D_{WBPN} is obtained from Eq. (10). As mentioned in section 2.2, the tail was not included in the CRM geometry, therefore,

to attain a value of drag that is more representative of a commercial aircraft, the drag component buildup method [17] was employed to estimate the tail drag, which was added to D_{WBPN} and D_{WB}.

The drag coefficient c_d can be defined by using the scaled CRM reference area A_{ref}, as follows:

$$C_d = \frac{D}{q_\infty A_{ref}} \quad (11)$$

where q_∞ is the dynamic pressure, defined as $0.5\rho_\infty V_\infty^2$. Similarly, the lift coefficient can be defined as:

$$C_l = \frac{L}{q_\infty A_{ref}} \quad (12)$$

The mass flow ratio MFR, is a reference parameter for the design of nacelles, and it is defined as the ratio between the streamtube captured area A_0 and the highlight area A_{hi}, which can be written as:

$$MFR = \frac{A_0}{A_{hi}} = \frac{m_0}{\rho_0 V_0 A_{hi}} \quad (13)$$

2.5 Aircraft lift and net propulsive force

In order to properly compare the aerodynamic performance of two different aircraft configurations, it is necessary that the lift coefficient C_l is the same and desirable that both configurations have a $F_{net} = 0$, so that the aircraft forces are balanced in the stream wise direction. Figure 5 shows the flowchart of the adopted procedure to obtain a target C_l and $F_{net} = 0\ N$. Initially, the commercial software GASTURB is utilized to carry out a thermodynamic cycle calculation, whose results are used to define the CFD boundary conditions. Next, a CFD simulation is performed for a guessed AoA and C_l is computed. The AoA is iterated until C_l reaches its target value. Subsequently, the mass flow at the fan face $\dot{m}_f$ is iterated until the condition $F_{net} = 0\ N$ is satisfied, for the same BPR. The target C_l used in this work was 0.5, the same as the CRM's. To accelerate the process and reduce the number of iterations, the variation in angle of attack ΔAoA is calculated by assuming a linear relation between AoA and C_l. Therefore, it was never necessary more than 3 iterations within the inner loop shown in figure 4, because two iterations provide the slope of the C_l versus AoA curve, which is used to calculate the final AoA. In the outer loop, 3 to 5 iterations were necessary to attain $F_{net} = 0\ N$. Despite of the significant number of iterations necessary for the aforementioned procedure, all of them can be done within the same CFD computation, not requiring the simulations to be reinitialized and hence convergence occurs rather quickly for each iteration.

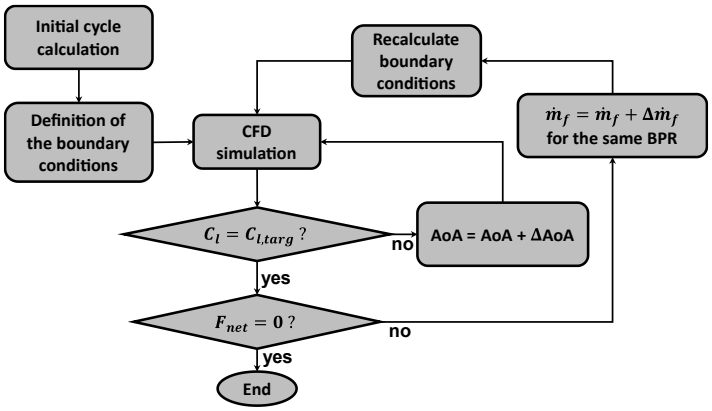

Figure 5 Flowchart to obtain a constant C_l and $F_{net} = 0\ N$ for the presented UWN and OWN configurations. $C_{l,targ} = 0.5$ in this study.

3.0 RESULTS AND DISCUSSION

3.1 Installation and interference effects on the wing

The CFD simulations were caried out using the procedure presented in Figure 5 to achieve $F_{net} = 0$ and $C_l = 0.5$. The OWN and UWN integrations are compared in terms of pressure distribution in Figure 6.

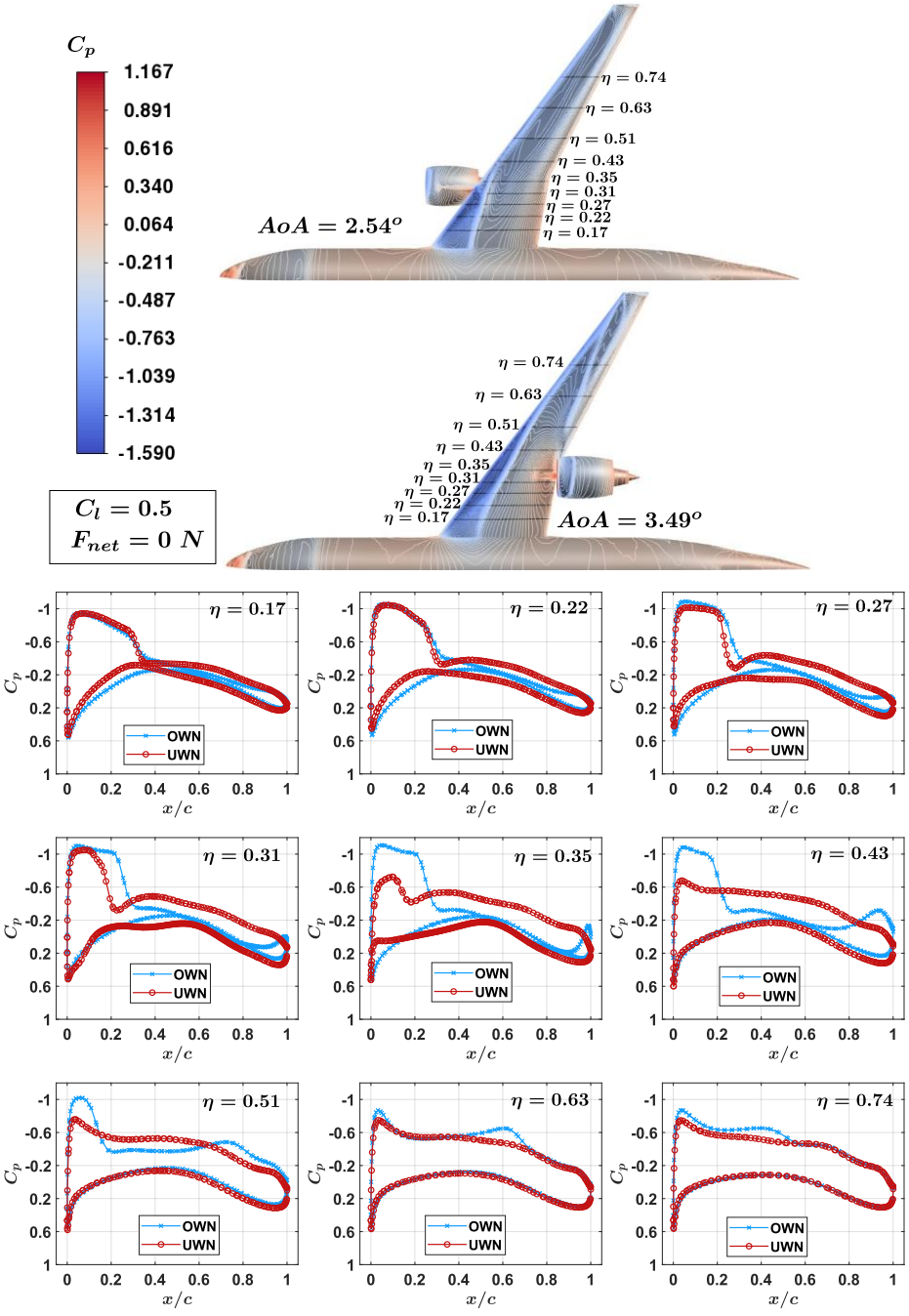

Figure 6 Contours of pressure coefficient and pressure distributions along the spanwise position for the OWN and UWN configurations. For both configurations $F_{net} = 0\ N$ and $C_l = 0.5$. The cruise Mach number is 0.8 and the altitude is 35000 ft. The AoA is equal to 2.54º and 3.49º for the UWN and OWN, respectively. η is the spanwise position relative to half of the wingspan

The UWN and OWN installations require AoA $= 2.54^o$ and AoA $= 3.49^o$ to achieve a lift coefficient equal to 0.5, respectively. The major reason for the higher OWN AoA are losses of lift caused by pressure disturbances created over the wings by the engines.

At cruise, the nacelles operate with a MFR lower than 1, meaning that the captured streamtube is diverging and diffusion occurs externally to the nacelle. Such phenomenon induces a higher pressure on the wing upper surface, contributing to a drop in lift for the same AoA. Moreover, a pressure rise can be observed near the OWN's pylon, which also adds to the loss of lift. For the UWN configuration, the aerodynamic impact of the captured streamtube is not that expressive (and maybe even negligible) since the engine is positioned upstream of the wing. It can be seen from the pressure contours shown in Figure 6 that the engine placement significantly interferes with the wing loading throughout the entire wingspan. Placing the engine under-the-wing initiates a strong shock on the inboard wing, which is gradually faded as the wingspan position is increased. The shock is the strongest near the wing station $\eta = 0.27$. For the OWN configuration the shock is slightly weaker than that of the UWN at the inboard side of the engine. However, outboard of the station $\eta = 0.27$ the OWN shock starts to become expressively stronger if compared with the UWN's, extending to a larger portion of the wingspan. It can be stated that the OWN configuration is able recover lift by increasing the overall shock strength on the wing upper surface, together with some increase in pressure at its lower surface ($\eta = 0.31$ to $\eta = 0.35$), likely due to absence of interference with the pylon. The overall increase in shock strength observed in the OWN configuration is likely to cause an increase in the overall drag. It can be seen that, at the wingspan stations $\eta = 0.31$ to $\eta = 0.43$, for the OWN configuration, an unusual pressure drop occurs near the wing training edge, and this seems to be induced by an interaction with the shock from the nacelle cowling.

3.2 Installation and interference effects on the nacelle

The Mach number contours around the wing and inlet ($\eta = 0.33$) are shown in Figure 7 for the a) UWN and b) OWN configurations. For the OWN configuration, the wing shock in expressively stronger than that of the UWN, as observed in the previous section. A weak shock can also be observed at the fan cowling's crown position for both the UWN and OWN cases. For the former, the shock forms after a small acceleration bubble, near the highlight, whereas, for the latter the supersonic bubble covers a wider portion of the cowl, and the shock appears near its axial position of maximum diameter. The UWN configuration would probably benefit from nacelle drooping or pitching to better align the incoming flow with the inlet, because some incidence can be observed in the incoming streamlines, mainly caused by wing upwash. For the OWN case, negative incidence is observed near the keel location, where the streamlines are moved downward due to wing downwash. On the other hand, at the crown position, the streamlines seem to have a low positive incidence relative to the inlet, therefore it is not clear if drooping the nacelle would be effective to decrease drag. It is possible that a negative droop or scarfing would be beneficial.

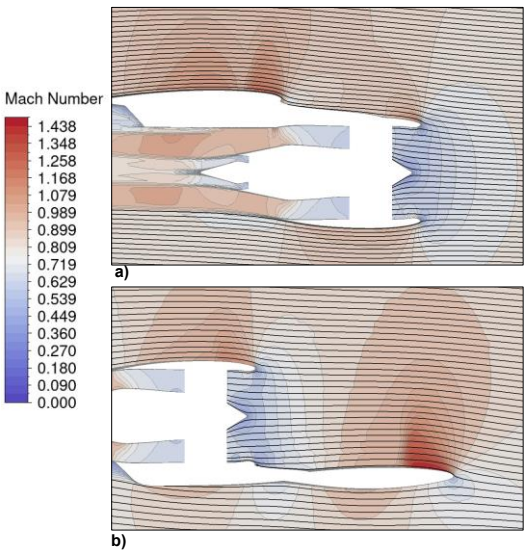

Figure 7 Mach number coutours around the wing and nacelle for the: a) UWN and b) OWN configurations. The spanwise position is $\eta = 0.33$ for both cases.

Figure 8 presents the contours of C_p for the inboard and outboard sides of the nacelle and pylon, along with the pressure distribution over different circumferential sections of the nacelle cowling. For the UWN configuration, a weak shock is formed at the upper portion of the fan cowling, covering majorly its outboard side, which seems to sweep an area between the circumferential stations $\theta = 135^o$ to $\theta = 270^o$. The remaining circumferential stations are shock free, since the acceleration occurs gradually, with no steep pressure gradients. For the OWN configuration, the shock is stronger and covers the entire cowl annulus. At the lower part of the cowling, the shock is the strongest at the inboard side, as it can be seen by comparing the pressure distributions at station $\theta = 15^o$ with $\theta = 345^o$ and $\theta = 45^o$ with $\theta = 315^o$. However, the shock grows weaker at the inboard side and stronger at the outboard side as it moves toward the upper part of the cowling, and this is clearly observable by comparing the pressure distribution at station $\theta = 135^o$ with $\theta = 225^o$, and $\theta = 165^o$ with $\theta = 195^o$. From the C_p contours in Figure 8, a strong interaction between the pylon and the nacelle shock can be observed for the OWN configuration. The presence of the pylon moves the shock upstream, at the lower part of the fan cowling, up to a position near the inlet's highlight. The cowling shock induces a low-pressure zone on the pylon creating a separation prone region. Such phenomenon does not occur for the UWN configuration. The observed stronger shock at the OWN configuration, together with a higher pylon/nacelle interference effect, might contribute to an increased installation drag.

3.3 Aerodynamic performance assessment

The bookkeeping methodology presented in section 2.4 was used to evaluate the aerodynamic performance of the OWN and UWN configurations. The values presented here are in terms of drag counts, or $10^4 \times C_d$. The major results obtained are shown in Table 1. The calculated wing body configuration drag C_d^{WB}, for $C_l = 0.5$, was 246.36 drag counts.

Table 1
Major aerodynamic performance results for the UWN and OWN configurations for $C_l = 0.5$ and $F_{net} = 0$ N.

	AoA (^{o})	C_d^{WBPN}	C_d^{inst}	C_d^{nac*}	C_d^{pylon}	C_d^A	MFR	L/D
UWN	2.54	283.13	36.76	40.61	1.21	241.31	0.773	17.65
OWN	3.49	302.80	56.44	22.40	6.04	274.36	0.783	16.51

The overall drag C_d^{WBPN} and installation drag C_d^{inst} were increased by 19.7 drag counts, when the engines were installed over-the-wings, compared to the conventional under-wing mount. The modified nacelle drag C_d^{nac*} is 18.21 drag counts lower for the OWN configuration, whilst the pylon drag C_d^{pylon} is 4.83 drag counts higher. Therefore, the higher OWN overall and installation drags can only be explained by a higher airframe drag C_d^A.The reason for a higher C_d^{nac*} obtained for the UWN configuration resides on the fact that the engine had to be throttled down to reach the $F_{net} = 0$ N condition. This decreased the MFR and thus increased ϕ_{pre} and spillage drag. Moreover, C_d^{pylon} was substantially increased in the OWN configuration, which, as discussed in section 3.2, was caused by its strong interference with the cowling's shock.

4.0 CONCLUSION

An integrated framework was used to evaluate the aerodynamic performance of an OWN configuration compared against a conventional UWN mount. The nacelle was designed by using class-shape-transformation (CST) curves, whereas the pylon geometries were generated by vertically stacking NACA 4-digit airfoils. The flow field was computed by means of RANS CFD and the aerodynamic performance of the configurations was assessed through bookkeeping of thrust and drag. It was found that, for the OWN configuration, the pressure disturbances generated on the upper wing surface, caused mainly by the captured streamtube diffusion, result in a loss in lift for the same AoA, therefore, for the same lift, a higher AoA is required, compared to the

UWN installation. The OWN case presented an inferior aerodynamic performance since its installation drag is 19.7 higher than that of the UWN configuration. The main reasons are: first, a significantly stronger wing shock for the OWN configuration, resulting in higher wave drag; and second, a higher pylon drag, caused by a strong interference with the shock at the fan cowling. Although the results presented here seem to reinforce the bad reputation acquired by OWN installation, they are far from enough to conclude that mounting the engines over-the-wings is not a viable integration choice. In fact, more advanced studies are still necessary. The installation of larger engines over-the-wings, which would not fit in a conventional under-wing installation, would allow for a better assessment of whether the loss in aerodynamic performance can be outweighed by a better engine propulsive efficiency. Moreover, carrying out more integrated multi-level optimizations, where the wing, nacelle and pylon shapes are varied along with the engine location, could lead to a significant improvement in aerodynamic performance.

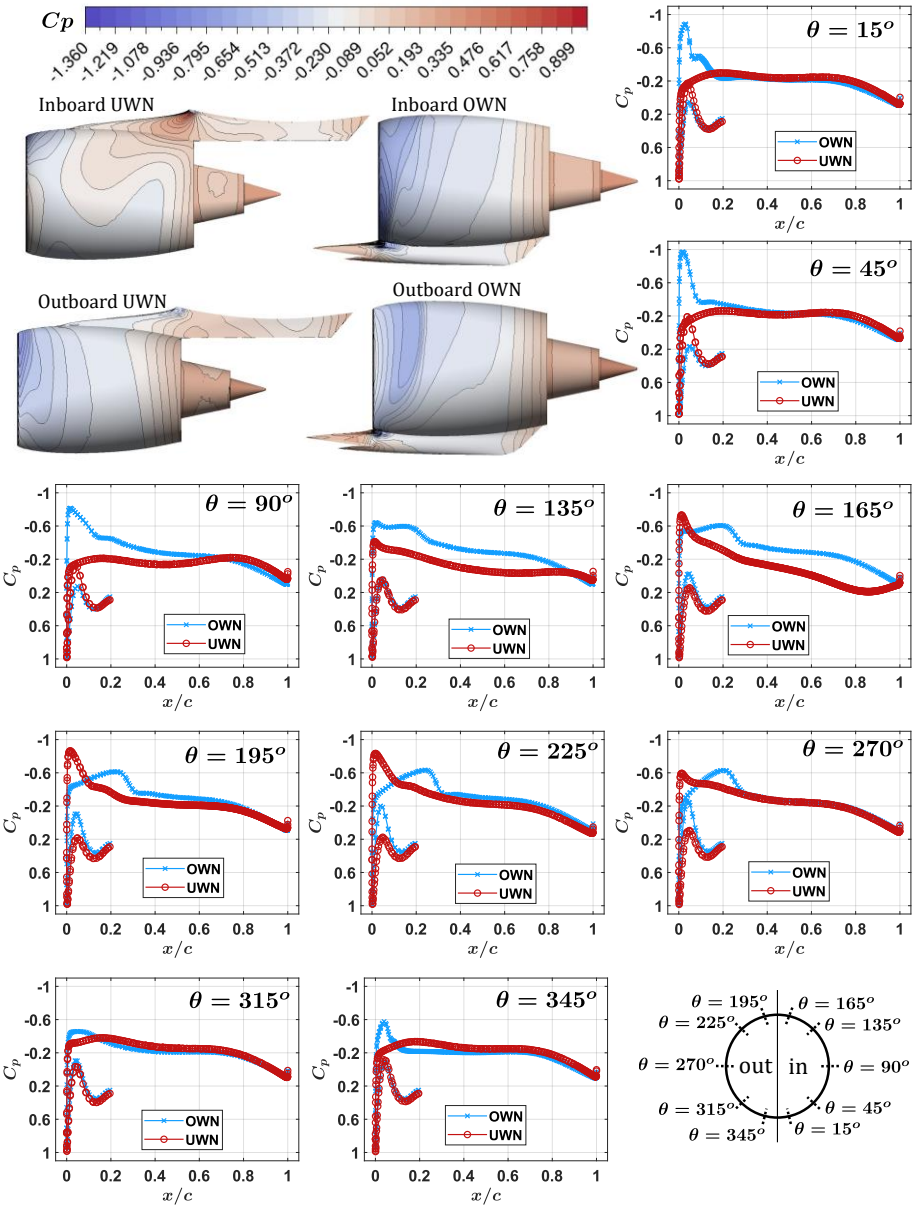

Figure 8 Contours of pressure coefficient and pressure distributions along the nacelle circumferential position θ for the OWN and UWN configurations. For both configurations $F_{net} = 0\ N$ and $C_l = 0.5$. The cruise Mach number is 0.8 and the altitude is 35000 ft. The AoA is equal to 2.54º and 3.49º for the UWN and OWN, respectively.

ACKNOWLEDGMENTS

This research work was funded by the Swedish National Aviation Engineering Research Program, NFFP, supported by Swedish Armed Forces, the Swedish Defense Materiel Administration, Swedish Governmental Agency for Innovation Systems (VINNOVA), and GKN Aerospace. All the computations were performed using Chalmers Center for Computational Science and Engineering (C3SE) resources, provided by Swedish National Infrastructure for Computing (SNIC).

REFERENCES

[1] D. Kinney, A. Hahn and P. Gelhausen, "Comparison of low and high nacelle subsonic transport configurations," in *15th Applied Aerodynamics Conference*, 1997.

[2] M. Fujino and Y. Kawamura, "Wave-Drag Characteristics of an Over-the-Wing Nacelle Business-Jet Configuration," *Journal of Aircraft,* vol. 40, no. 6, pp. 1177-1184, 2003.

[3] G. A. Hill and O. A. Kandil, "Aerodynamic Investigations of an Advanced Over-the-Wing Nacelle Transport Aircraft Configuration," in *45th AIAA Aerospace Sciences Meeting and Exhibit*, Nevada, 2007.

[4] S. H. Berguin and D. N. Mavris, "Interactions in Over-Wing Nacelle Optimization," in *51st AIAA Aerospace Sciences Meeting including the New Horizons Forum and Aerospace Exposition*, Grapevine, 2013.

[5] J. R. Hooker, A. Wick, C. Zeune and A. Agelastos, "Over Wing Nacelle Installations for Improved Energy Efficiency," in *31st AIAA Applied Aerodynamics Conference*, San Diego, 2013.

[6] M. Lorteau, L. Wiart, V. Kopiev and S. Denisov, "Numerical study, with experimental validation, of fan noise installation effects in Over-Wing Nacelle configuration using the Immersed Boundary Method," in *25th AIAA/CEAS Aeroacoustics Conference*, 2019.

[7] J. R. Hooker and A. Wick, "Design of the Hybrid Wing Body for Fuel Efficient Air Mobility Operations," in *52nd Aerospace Sciences Meeting*, 2014.

[8] A. Magrini, D. Buosi and E. Benini, "Maximisation of installed net resulting force through multi-level optimisation of an ultra-high bypass ratio engine nacelle," *Aerospace Science and Technology,* vol. 119, pp. 1-18, 2021.

[9] I. Goulos, J. Otter, F. Tejero, J. Hueso Rebassa, D. M. Manus and C. Sheaf, "Civil turbofan propulsion aerodynamics: Thrust-drag accounting and impact of engine installation position," *Aerospace Science and Technology,* vol. 111, pp. 1-14, 2021.

[10] B. M. Kulfan, "Universal parametric geometry representation method," *Journal of aircraft,* vol. 45, no. 1, pp. 142-158, 2008.

[11] F. Zhu and N. Qin, "Intuitive Class/Shape Function Parameterization for Airfoils," *AIAA Journal,* vol. 52, no. 1, pp. 17-25, 2014.

[12] V. T. Silva, A. Lundbladh, O. Petit and C. Xisto, "Multipoint Aerodynamic Design of Ultrashort Nacelles for Ultrahigh-Bypass-Ratio Engines," *Journal of Propulsion and Power,* pp. 1-18, 2022.

[13] J. Vassberg, M. Dehaan, M. Rivers and R. Wahls, "Development of a Common Research Model for Applied CFD Validation Studies," in *26th AIAA Applied Aerodynamics Conference*, Honolulu, 2008.

[14] Ministry-Industry Drag Analysis Panel (MIDAP) Study Group, "Guide to In-Flight Thrust Measurement of Turbojets and Fan Engines," AGARDograph No. 237, 1979.

[15] D. Destarac and J. v. d. Vooren, "Drag/thrust analysis of jet-propelled transonic transport aircraft; Definition of physical drag components," *Aerospace Science and Technology* , vol. 8, no. 6, p. 545–556, 2004.

[16] B. Malouin, J.-Y. Trépanier and É. Laurendeau, "Installation and interference drag decomposition via RANS far-field methods," *Aerospace Science and Technology*, vol. 54, pp. 132-142, 2016.

[17] D. P. Raymer, Aircraft Design: A Conceptual Approach, American Institute of Aeronautics and Astronautics, Inc., 2018.